PHYSICAL REVIEW LETTERS

Atomic-Resolution Imaging with a Sub-50-pm Electron Probe

Rolf Erni, Marta D. Rossell, Christian Kisielowski, and Ulrich Dahmen

National Center for Electron Microscopy, Lawrence Berkeley National Laboratory, Berkeley, California 94720, USA
(Received 17 June 2008; published 2 March 2009)

Using a highly coherent focused electron probe in a fifth-order aberration-corrected transmission electron microscope, we report on resolving a crystal spacing less than 50 pm. Based on the geometrical source size and residual coherent and incoherent axial lens aberrations, an electron probe is calculated, which is theoretically capable of resolving an ideal 47 pm spacing with 29% contrast. Our experimental data show the 47 pm spacing of a Ge ⟨114⟩ crystal imaged with 11%–18% contrast at a 60%–95% confidence level, providing the first direct evidence for sub-50-pm resolution in annular dark-field scanning transmission electron microscopy imaging.

Recent advances in aberration-correcting electron optics have made sub-angstrom imaging in transmission electron microscopy almost routine in both the broad beam and the scanning probe modes [1–4]. The desire to further improve the spatial resolution in electron microscopy is driven in large part by the need for increased sensitivity, image contrast [5], and atomic-resolution tomography [6]. In this Letter, we report on utilizing a new generation aberration-corrected microscope to form a highly coherent sub-50-pm electron probe at 300 kV and demonstrate that this probe is capable of resolving the 47 pm dumbbell spacing in a Ge ⟨114⟩ crystal.

In scanning transmission electron microscopy (STEM), the size of the electron probe that is focused onto the specimen ultimately limits the spatial resolution. Apart from mechanical and electrical stability, the size of the probe is determined by the illumination half-angle α, residual coherent axial aberrations, and incoherent broadening due to partial temporal and partial spatial coherence given by the finite energy length and the finite size of the demagnified electron source, respectively.

Previous efforts to improve the spatial resolution in STEM have mainly focused on minimizing phase shifts caused by lens aberrations in order to increase the illumination angle and, hence, to reduce the impact of the diffraction limit on the lateral resolution. Strategies to optimize the electron probe by improving the electron-optical setup have largely neglected the finite size of the electron source, thus implying infinite source brightness and demagnification. Here we consider the effect of the finite size of the electron source using the geometrical source size, which corresponds to the size of the demagnified electron source that is imaged onto the specimen.

For a given electron energy E_0, the coherent point source contribution to the electron probe in the aperture plane can be expressed as

$$\psi(\omega) = \exp\left(\frac{2\pi i}{\lambda}\chi(\omega)\right)\left[1 + \exp\left(\frac{\omega\omega^* - \alpha^2}{\delta_\alpha^2}\right)\right]^{-1}. \quad (1)$$

The complex coordinate in the aperture plane is ω, ω^* is its complex conjugate, $\lambda = \lambda(E_0)$ is the electron wavelength, and $\chi(\omega)$ is the aberration function [7]. The first term expresses aberration phase shifts, and the second term is the aperture function. The parameter δ_α can be chosen as a small fraction of α in order to minimize artifacts that can arise in the numerical treatment of $\psi(\omega)$ when a sharp edge function is considered [8].

By knowing the brightness β of the electron source, the current of the electron probe I_P, and the angle α, the geometrical source size d_{geo} (FWHM) can be estimated by $d_{geo}^2 = 4I_P/(\pi^2\alpha^2\beta)$ [9]. To incorporate the effect of partial spatial coherence, we assume a Gaussian source distribution function

$$S(w) = \frac{1}{\sqrt{2\pi\sigma_S^2}}\exp\left(-\frac{ww^*}{2\sigma_S^2}\right). \quad (2)$$

The standard deviation σ_S is related to d_{geo} by $\sigma_S^2 = d_{geo}^2/8\ln2$, and $w = x + iy$ denotes the complex coordinate in the specimen plane. The probe intensity is then expressed by $|\psi(w)|^2 \otimes S(w)$, where $\psi(w)$ is the Fourier transform of $\psi(\omega)$ and $\otimes$ denotes convolution.

Partial temporal coherence leads to an additional incoherent broadening of the electron probe. This effect is determined by the energy spread of the source and the constant of chromatic aberration C_C. Because of the variation δE of electron energies around E_0, the chromatic aberration causes a variation of the defocus C_1 given by $\delta C_1 = C_C\delta E/E_0$ which directly affects the aberration function $\chi(\omega)$ in Eq. (1). Hence, the probe wave field $\psi(w)$ becomes a function of energy E. The intensity of the electron probe is then given by

$$I(w) = \int_{-\infty}^{\infty}\left[|\psi(w, E)|^2 \otimes S(w)\right]\frac{dT(E)}{dE}dE, \quad (3)$$

with

$$\frac{dT(E)}{dE} = \frac{1}{\sqrt{2\pi\sigma_T^2}} \exp\left(-\frac{(E-E_0)^2}{2\sigma_T^2}\right). \qquad (4)$$

Equation (4) describes a Gaussian distribution of electron energies E around E_0 with $\sigma_T^2 = \Delta E^2/8\ln 2$, and ΔE is the FWHM of the energy spread [7].

Calculating a 300 keV aberration-free ($\chi = 0$) electron probe according to Eq. (3) for $\alpha = 28.9$ mrad and $d_{geo} = 50$ pm, considering partial temporal coherence due to an energy length $C_C\Delta E$ of 1.68 mm eV, yields a probe intensity profile of 53 pm FWHM. Reducing the energy length by a factor of 2 results in a probe of 47 pm, whereas a reduction of d_{geo} by a factor of 2 shrinks the probe to less than 38 pm. Thus the effect of d_{geo} on the probe size highlights the importance of source brightness and partial spatial coherence [10] in STEM imaging.

In this work, we present evidence for a sub-50-pm electron probe formed in a new generation aberration-corrected transmission electron microscope that has been developed as part of the TEAM (transmission electron aberration-corrected microscopy) project [11]. The TEAM 0.5 microscope is equipped with a novel Schottky-type high-brightness field-emission electron source and an improved hexapole-type illumination aberration corrector [12]. The brightness β of the electron source was $\sim 3.8 \times 10^9$ A/(cm^2 srad) at 300 kV. We employed an electron probe of $I_P = 46$ pA at an illumination half-angle α of 28.9 mrad, implying a geometrical source size of ~ 25 pm. The probe corrector enables the correction of aberrations up to fifth-order spherical aberration C_5. The following aberration coefficients were measured (for notation see, e.g., [7]): $A_2 = 24$ nm, $B_2 = 8$ nm, $C_3 = -149$ nm, $A_3 = 97$ nm, $S_3 = 90$ nm, $A_4 = 10.2$ μm, $D_4 = 7.2$ μm, $B_4 = 5.5$ μm, $C_5 = 509$ μm, $A_5 = 221$ μm, $S_5 = 7$ μm, and $R_5 = 24$ μm [11]. Defocus C_1 and twofold astigmatism A_1 were manually optimized.

The illumination angle was chosen in order to balance the impact of the diffraction limit against residual coherent aberrations and, considering the finite energy length of 1.68 mm eV, to minimize probe tails that arise if a too large angle is chosen.

Figure 1(a) presents an annular dark-field (ADF) STEM micrograph of a Ge foil in ⟨114⟩ zone axis orientation that was recorded with an electron probe having the characteristics described above. The ⟨114⟩ projection of Ge consists of a periodic array of pairs of atom columns that are separated by 47 pm. Because of glide-mirror symmetry, the two columns of atoms forming the dumbbell are shifted with respect to each other by 0.47 nm in the direction of projection. The crystal planes corresponding to the 47 pm distance are of the type {884}. Atoms along each column are separated by 1.2 nm.

The micrograph was recorded using a magnification corresponding to a Nyquist frequency of 50.2/nm (9.95 pm/pixel), a dwell time of 7 μs, and an annular detection range of ~ 45–290 mrad (semiangle). The signal amplifier was adjusted to utilize the full dynamic range of the detector without clipping the signal. The Ge specimen was cut in a ⟨114⟩ orientation from a ⟨001⟩-Ge wafer and mechanically polished, followed by Ar ion milling. The estimated sample thickness is ~ 10 nm.

Figure 1(b) shows the micrograph after high-frequency noise reduction using a low-pass filter set at 40 pm with the edge of the Fourier mask smoothed from 32 and 40 pm. Single-pixel line profiles along the atom row of the region of interest (RoI) 1 in Fig. 1(a) and of the equivalent row from the filtered micrograph in Fig. 1(b) are shown in Fig. 2(a). The power spectrum and the line profiles in Fig. 2 confirm the presence of the $88\bar{4}$ image frequency as well as other sub-50-pm reflections. The $\bar{8}80$ reflection (50 pm) in the direction perpendicular to $[44\bar{2}]$ is weakly present but falls into an area of the power spectrum that is affected by residual scan noise.
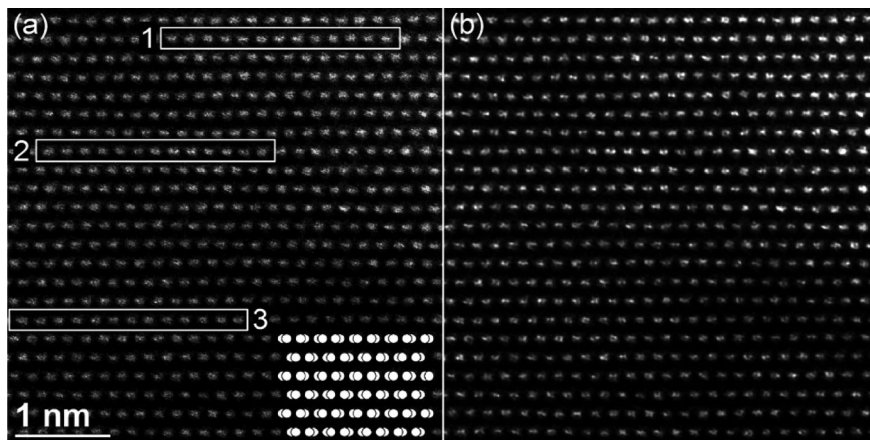

FIG. 1. ADF STEM micrograph of Ge ⟨114⟩ with overlaid model. (a) Raw data; (b) after high-frequency noise reduction using a smooth low-pass filter set at 40 pm. The area corresponds to about a quarter of the original micrograph rotated by 22.3°.

From Fig. 1 and the line profile in Fig. 2(a), it is clear that the 47 pm dumbbell splitting is observed locally but not everywhere because the micrograph is affected by noise. In the presence of noise, resolution depends on the significance with which a signal can be detected above the noise level [13]. In order to quantitatively assess the noise level as well as the statistical relevance of the sub-50-pm information, we performed local statistical analyses for the RoIs in Fig. 1(a). For each of the three RoIs, we derived the average dumbbell structure and the corresponding noise. The line profiles in Fig. 3(a) across the averaged structures reveal dips of 11%, 18%, and 8% contrast for RoI 1, 2, and 3, respectively.

The averaged structure of RoI 1 is shown in Fig. 3(c). The error bars in Fig. 3(a) are the standard deviations obtained by comparing the individual dumbbells with the averaged structures [14]. From the standard deviation for each pixel, the dumbbell dip can be characterized with a confidence level. The 11% dumbbell contrast in RoI 1 is measured with a confidence level of 60%, while the 18% contrast in RoI 2 has a confidence level of 95%. These confidence levels reflect the statistical significance of observing the 47 pm splitting in individual image unit cells. By comparison, RoI 3 shows only 8% contrast with a confidence level of merely 1%, indicating that in this area the dumbbell spacing has not been resolved. However, the result of RoI 1 and 2 provides clear evidence supporting the presence of a sub-50-pm electron probe and the 47 pm instrument resolution.

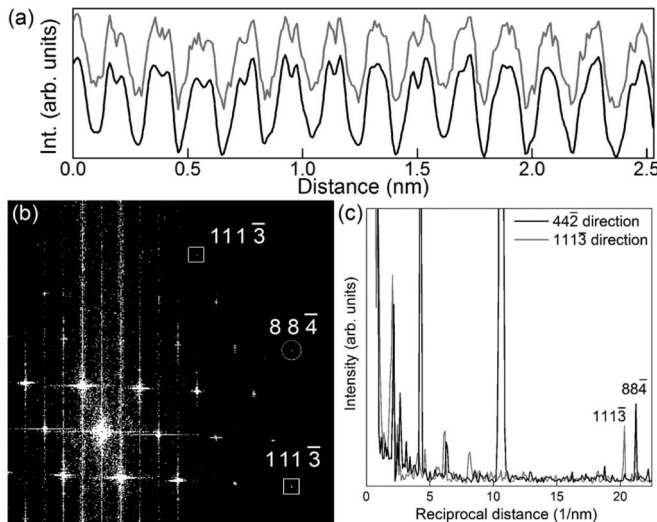Electron-probe calculations according to Eq. (3) for an energy length of 1.68 mm eV yield a theoretical electron probe of 41 pm FWHM, assuming that the overall instrument stability preserves the brightness from source to specimen. Instabilities of high temporal frequency would lead to an effective blurring of d_{geo} [15], whereas instabilities of lower frequencies would cause apparent scan noise. For an object that consists of two delta functions separated by 47 pm, the theoretical contrast can be found by convoluting the idealized object with the calculated electron probe; see Fig. 3(b). The line profile of the calculated dumbbell in Fig. 3(a) reveals a dip of 29%, representing the instrument resolution achievable for the theoretical electron probe and an idealized 47 pm spacing.

Comparing theoretical instrument resolution with an experimental micrograph raises the question of the extent to which the specimen limits the observable resolution. The local variation of the experimentally observed 47 pm contrast can be explained by residual low-frequency instrument instabilities and particularly by specimen imperfections, including the presence of amorphous surface layers, surface roughness, or point defects. Such imperfections can be caused by ion milling during sample thinning, adsorbates from the environment, or beam damage during electron exposure. Amorphous layers lead to a reduction in contrast as well as local variations in intensity. Although beam damage is unlikely to generate point defects in bulk Ge at 300 keV [16], radiation damage of the more weakly bound surface atoms can still occur, causing roughness or amorphous layers at the surface.

FIG. 2. (a) Line profiles across the atom row of RoI 1 in Fig. 1 (a) (gray) and Fig. 1(b) (black). (b) Detail of the power spectrum of the Ge ⟨114⟩ micrograph and (c) line profiles through the power spectrum. The 88$\bar{4}$ image frequency (47 pm) and both 111$\bar{3}$-type reflections (49 pm) are present, confirming the sub-50-pm information transfer.
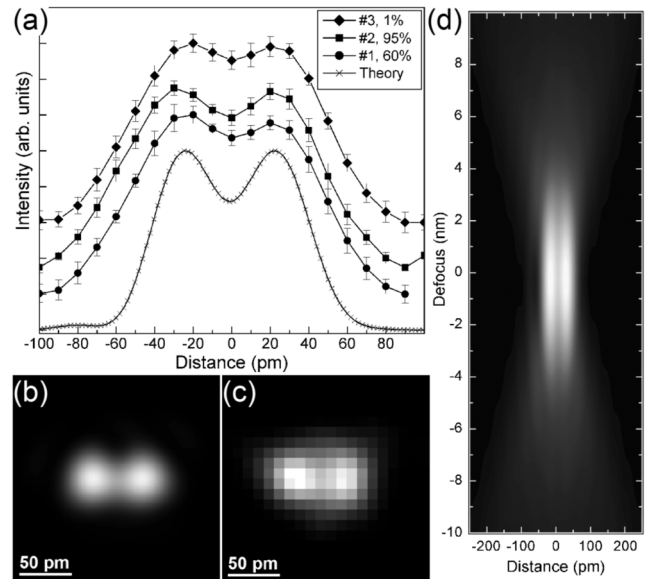

FIG. 3. (a) Single-pixel line profiles across the averaged dumbbell structures derived from RoIs 1, 2, and 3 in Fig. 1(a). The theoretical curve in (a) is a line profile across the calculated dumbbell in (b), showing that the 47 pm spacing can be resolved with 29% contrast for zero defocus. (c) Averaged dumbbell structure derived from RoI 1 in Fig. 1(a). (d) Defocus dependence of the 47 pm dumbbell contrast.

Apart from specimen imperfections, the optics of a small electron probe also restricts the achievable contrast. In order to reduce the impact of the diffraction limit on the (lateral) spatial resolution in STEM imaging, a large (aberration-free) illumination angle is desirable. However, working with a highly convergent electron probe in ADF STEM imaging substantially reduces the depth of field. While this gives access to 3D information [17], it reduces the thickness regime that is "in focus" if one is interested solely in projected 2D lateral information. For a crystal of a given density, a finer atomic spacing in the plane of projection implies a larger atomic spacing along the axis of projection. In the Ge ⟨114⟩ projection, atoms in each column are separated by 1.2 nm in the depth direction. A calculation of the 47 pm dumbbell image, similar to Fig. 3(b) but as a function of defocus, assuming purely incoherent imaging and no channeling effects, shown in Fig. 3(d), reveals the focus dependence of the contrast of the 47 pm spacing. Even for small defocus of only ±3 nm, the theoretical contrast of the 47 pm spacing drops from 29% to below 10%. Because of this limited depth of field, the dumbbell spacing can be resolved only within a narrow focus range of ~4–5 nm. This defines the crystal slice that makes the most important contribution to the ADF STEM micrograph. It can be concluded that, under these conditions of focal depth and interatomic spacing along the beam direction, there are only 3–4 pairs of atoms that provide substantial contrast to the dumbbell image. Areas above and below the 4.5 nm slice reduce the attainable 47 pm contrast.

The points discussed above are based on the assumption that the size of the object is negligible. However, the size of the object is finite, although the width of the atom columns that is relevant for electron scattering in STEM imaging remains an unresolved issue. Whether the width of an atom column is determined by the scattering cross section of an individual atom or alternatively by the column's $1s$ state [18], the finite size of the object reduces the contrast [2]. But even if the size of the object is not quantifiable, its displacement from the equilibrium position can affect the resolution. Because the time for an electron to traverse the specimen is short compared to a phonon vibration, each electron experiences a different crystal configuration [19]. The root-mean-square displacement of Ge at 300 K is of the order of ~8–9 pm [20], clearly sufficient to impact the 47 pm dumbbell contrast.

In conclusion, we have presented evidence for a sub-50-pm electron probe at 300 kV that made it possible to resolve the 47 pm spacing of Ge ⟨114⟩ in ADF STEM imaging. It is shown that the goal of forming smaller electron probes is not achievable solely by improving the aberration-corrected optics. The brightness of the electron source and the geometrical source size are crucial parameters that ultimately limit the size of the electron probe.

Furthermore, the statistical analysis of the Ge ⟨114⟩ micrograph underlines the importance of experimental noise in the discussion of resolution. We discuss the discrepancy between theoretically possible and experimentally observed image contrast in terms of the influence of random noise, the finite size of the object, the limited depth of field, and imperfections in the specimen. From this analysis we conclude that the sub-50-pm resolution presented here is not limited by the electron-optical setup.

[1] P. E. Batson, N. Dellby, and O. Krivanek, Nature (London) **418**, 617 (2002).
[2] P. D. Nellist *et al.*, Science **305**, 1741 (2004).
[3] M. Haider *et al.*, Nature (London) **392**, 768 (1998).
[4] H. Sawada *et al.*, Jpn. J. Appl. Phys. **46**, L568 (2007).
[5] J. C. Meyer *et al.*, Nano Lett. **8**, 3582 (2008).
[6] J. R. Jinschek *et al.*, Ultramicroscopy **108**, 589 (2008).
[7] M. Haider, S. Uhlemann, and J. Zach, Ultramicroscopy **81**, 163 (2000).
[8] E. J. Kirkland, R. F. Loane, and J. Silcox, Ultramicroscopy **23**, 77 (1987).
[9] M. Born and E. Wolf, *Principles of Optics* (Cambridge University Press, Cambridge, England, 2003), 7th ed.
[10] C. Dwyer, R. Erni, and J. Etheridge, Appl. Phys. Lett. **93**, 021115 (2008).
[11] C. Kisielowski *et al.*, Microsc. Microanal. **14**, 469 (2008).
[12] H. Müller *et al.*, Microsc. Microanal. **12**, 442 (2006).
[13] S. Van Aert, D. Van Dyck, and A. J. den Dekker, Opt. Express **14**, 3830 (2006).
[14] The standard deviations measured include both random and systematic noise. The variations of the local minima between the dumbbell pairs in Fig. 2(a) reflect the systematic low-frequency noise. Frequency-dependent noise analysis revealed that random and systematic noise contribute in equal proportion. Since the systematic error is not relevant for the dumbbell resolution, the errors in Fig. 3(a) reflect random noise only.
[15] The impact of high-frequency noise on the geometrical source size can be incorporated by considering an effective geometrical source size $d^2_{\mathrm{geo,eff}} = d^2_{\mathrm{geo}} + d^2_{\mathrm{noise}}$.
[16] J. J. Loferski and P. Rappaport, Phys. Rev. **111**, 432 (1958).
[17] K. van Benthem *et al.*, Ultramicroscopy **106**, 1062 (2006).
[18] P. Geuens and D. van Dyck, Ultramicroscopy **93**, 179 (2002).
[19] J. M. Cowley, Appl. Phys. Lett. **15**, 58 (1969).
[20] V. F. Sears and S. A. Shelley, Acta Crystallogr. Sect. A **47**, 441 (1991).